
Document Number**:** H2020-ICT-52/RISE-6G/D7.1

Project Name:
**R**econfigurable **I**ntelligent **S**ustainable **E**nvironments for **6G** Wireless Networks
(RISE-6G)

# Deliverable D7.1

# Integration methodology and impact measurements through advanced KPIs

Date of delivery: 27/09/2022 Version: 2.0
Start date of Project: 01/01/2021 Duration: 36 months

# Deliverable D7.1

# Integration methodology and impact measurements through advanced KPIs

| | |
|---|---|
| **Project Number**: | 101017011 |
| **Project Name:** | **R**econfigurable **I**ntelligent **S**ustainable **E**nvironments for **6G** Wireless Networks |

| | |
|---|---|
| **Document Number**: | H2020-ICT-52/RISE-6G/D7.1 |
| **Document Title:** | Deployment and control strategies of RIS based connectivity (Intermediary Specifications) |
| **Editor(s):** | ZHONGXIA SIMON HE (Chalmers) |
| **Authors:** | Simon He Zhongxia (CHAL), Vincenzo Sciancalepore (NEC), Placido Mursia (NEC), Raffaele D'Errico (CEA), Antonio Clemente (CEA), Paolo Gianola (TIM), Jean-Baptiste Gros (GNW), Luca Bastianelli (CNIT), Maurizio Crozzoli (TIM), Dinh-Thuy Phan-Huy (ORA), Petar Popovski (AAU), Fabio Saggese (AAU) |
| **Dissemination Level:** | PU |
| **Contractual Date of Delivery:** | 30/06/2022 |
| **Security:** | Public |
| **Status:** | Draft |
| **Version:** | 2.0 |
| **File Name:** | |



**Abstract**

In this deliverable, the experimental hardware and setup for RIS prototypes are described, including available instruments and test environments. Different application use cases including communication and localization are defined. RIS protypes are validated for communication and localization use cases separately, which cover a wide frequency range from sub-6 GHz to 150 GHz. RIS integration plan considering different use cases towards expected field-trials is also described.

**Keywords**

*Beyond-5G; 6G; RIS; Scenarios; Experimental validation, communication, localization*

# Contents

# List of Figures

# List of Acronyms

| | |
|---|---|
| 5G-NR | 5th Generation - New Radio |
| BER | Bit Error Rate |
| BS | Base Station |
| CAPEX | CAPital EXpenditure |
| CE | Channel Estimation |
| CSI | Channel State Information |
| DL | Downlink |
| DL-DoD | Downlink Direction of Departure |
| DL-TDoA | Downlink Time Difference of Arrival |
| DoA | Direction of Arrival |
| DoD | Direction of Departure |
| DRL | Deep Reinforcement Learning |
| EM | Electromagnetic |
| GDoP | Geometric Dilution of Precision |
| HRIS | Hybrid Reconfigurable Intelligent Surface |
| KPI | Key-Performance Indicator |
| LB-AoI | Localization Boosted - Area of Influence |
| LE-AoI | Localization Enabled - Area of Influence |
| LoS | Line-of-Sight |
| MIMO | Multiple Inputs Multiple Outputs |
| MISO | Multiple Inputs Single Output |
| MSE | Mean Squared Error |
| NMSE | Normalised Mean Squared Error |
| NVAA | Non-Value-Added Activities |
| OFDM | Orthogonal Frequency Division Multiplexing |
| OPEX | OPerating EXpenditure |
| PARAFAC | PARAllel FACtor |
| RF | Radio Frequency |
| R-RIS | Reflective RIS |
| RT-RIS | Reflective-transmission RIS |
| RIS | Reconfigurable Intelligent Surface |
| RSSI | Received Signal Strength Indicator |
| RTT | Round Trip Time |
| RT-ToF | Round Trip – Time of Flight |
| Rx | Receiver |
| SINR | Signal to Interference plus Noise Ratio |
| SISO | Single Input Single Output |
| SLAM | Simultaneous Localization and Mapping |
| SNR | Signal to Noise Ratio |
| TDoA | Time Difference of Arrival |
| ToA | Time of Arrival |
| Tx | Transmitter |
| UAV | Unmanned Aerial Vehicle |
| UE | User |
| UTDoA | Uplink Time Difference of Arrival |
| UL | Uplink |
| UL-DoA | Uplink Direction of Arrival |
| UL-TDoA | Uplink Time Difference of Arrival |

# 1 Introduction

The general objective of the RISE-6G WP7 is the analysis and design of an overall RIS-based solution that encompasses different RIS-empowered equipment together with advanced transmitters and receivers to build new-generation wireless networks. In particular, it will be obtained by assembling RIS components and fine-tuning realistic equipment settings. Additionally, WP7 will validate innovations and demonstrate the feasibility of technological proposals by means of two different field-trials. This deliverable serves the first step that summarizes main RIS-based Proof-of-Concepts analysed and developed in WP3 in the perspective of their functionalities in different use scenarios.

The general objectives of this deliverable can be summarized as follows:

- Validation of various RIS components including S-band, Ka-band, V-band and D-band, up to 130 GHz;
- Development of RIS components that will be integrated into a unified solution for generic communication applications;
- Development of RIS components that will be integrated into a unified solution for generic localization applications.

This deliverable is structured as following: after introduction, the RIS test equipment and available hardware are listed in Section 2; RIS prototypes developed at different frequency bands are descibed in Section 3. The RIS prototype functional test for communication use case is presented in Section 4 and functional test for localization use case is demonstrated in Section 5. Finally, Section 6 provides the conclusions and the summary.

## 1.1 Definition of application scenarios

Two main application scenarios are defined for RIS deployments in future PoC and demonstrators: enhancing communication coverage and facilitating and improving localization accuracy. For the communication application, the typical scenario is illustrated in
Figure 1-1. For millimetre-wave communication, due to limited output power, transceiver nodes often use high directional antennas. This implies a line-of-sight (LoS) communication which limits the deployment flexibility in actual applications. Obstacle objects may move between LoS and block or reduce the communication quality of such communication links. The RIS can be deployed on the side of LoS path, when main LoS path is block it can be used to rely and recover communication based on reflection principle. For different communication devices at different operational band, corresponding RIS components are required. The RIS controlling strategy, RIS deployment density and location should be analysed case by case considering the frequency band characteristic and RIS prototype performance.

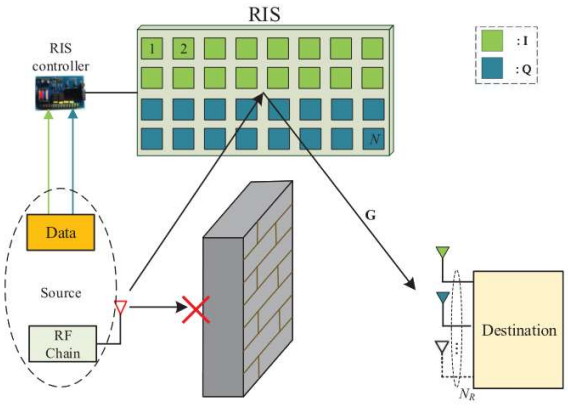


**Figure 1-1. RIS application scenario for communication use case**

To deploy localization-related use cases, the RIS can be exploited to form a virtual scanning beam as shown in Figure 1-2. In a traditional MIMO radar structure, separate radar transceiver channel has to be placed with half wavelength spacing in order to form beamforming configuration. For high frequency bands, the antenna element separation gets very limited such that it becomes physically challenging to place full radar transceiver channels in practise. Furthermore, high frequency band transceivers have higher cost and power consumption, therefore traditional MIMO radar concept become less attractive. Using RIS to reflect single radar beam to certain direction can enable high directional virtual scanning beam that enables accurate localization with limited number of expensive millimeter wave transceivers.

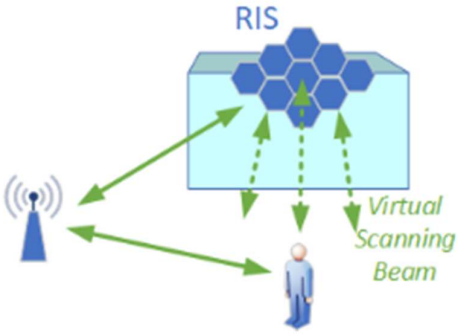


**Figure 1-2. RIS application scenario for localization use case**

# 2 Experimental Hardware for RIS validation

## 2.1 Reverberation chamber for tests

For testing wireless devices, such as the 5G base station (BS), we use the reverberation chamber (RC) situated at CNIT laboratory in Ancona university. This facility has already been used for emulating real life scenarios in order to evaluate 4G-LTE system performance [BMB+17, MBM+15, MBC+16, MBD+18, MBB+20, BMD+17, BMG+14]. Figure 2-1 shows in details the interior of the considered reverberation chamber.

**Figure 2-1. Reverberation chamber (RC) used during tests. It is equipped with two stirrers, absorbing materials and, in this case, with the 5G BS module operating at the mmWave. In addition, on the left side of the chamber there is also the 4G-LTE and 5G (sub-6 GHz) RF modules. Moreover, the user equipment is located within the RC and it is connected to a personal computed that collects recorded data.**

The reverberation chamber has dimensions 6x4x2.5 $m^3$. During tests, we can adjust the load within the RC, by adding or removing pyramidal absorbers. In this way, the RC can be opportunely tuned to emulate the desired environment characterized by proper parameters of a multipath environment, such as the power delay profile and time delay spread [BGM+15, GHR+10]. The RISs will be placed in different positions within the RC to exhaustively test the frequency selectiveness.
Moreover, the effect of the RIS on multipath fading and interference mitigation will be investigated in FR1 band operating the Greenerwave-Nottingham SDR platform within the large RC facility of CNIT-Ancona, effectively scaling up the tests conducted tests in [GLL+22, LGG+22].

## 2.2 4G/5G NSA coverage equipment for lab tests and trials

### 2.2.1 4G/5G (NSA) Base Station

We consider the eNode-B and gNode-B as shown in Figure 2-2. Such base stations are effectively installed at CNIT labs in Ancona.

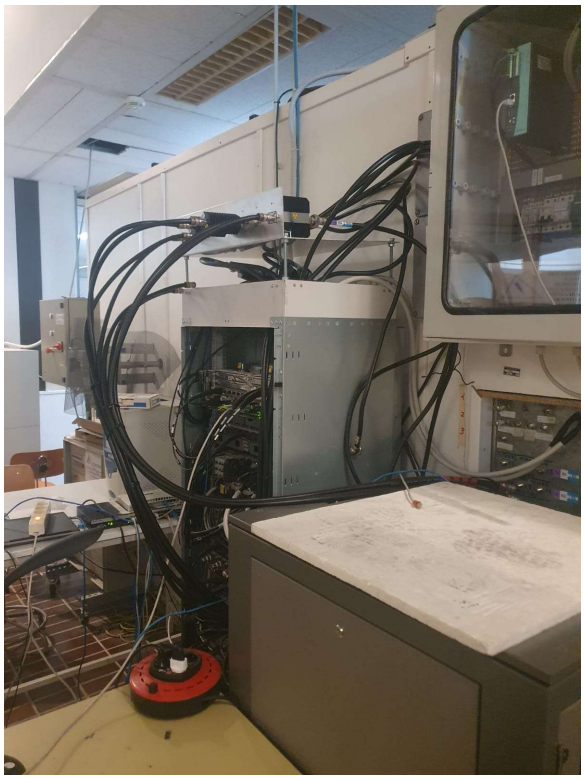

**Figure 2-2. 5G Base Station**

### 2.2.2 Sub-6GHz 5G RF module

The 5G RF module operating at N78 band (licensed TIM frequency band is 3720-3800 MHz) installed at CNIT labs in Ancona is shown in Figure 2-3.

**Figure 2-3. Sub-6GHz 5G RF module**

### 2.2.3 mmWaves 5G Base Station

The 5G RF module of Figure 2-4 operates at N258 band (licensed TIM frequency band is 26.9-27.1 GHz) and is installed at CNIT labs in Ancona.

**Figure 2-4. mmWaves 5G RF module**

### 2.2.4 4G Base Station

The 4G RF modules operating at B1, B3 and B7 bands are installed at CNIT labs in Ancona as 5G anchor layer and are depicted in Figure 2-5.

**Figure 2-5. 4G RF modules**

### 2.2.5 5G User Equipment

User Equipment (UE) is depicted in Figure 2-6 and is installed at CNIT labs in Ancona for enabling end-to-end (E2E) tests.


**Figure 2-6. 5G User Equipment**

## 2.3 Hardware Equipment for localization validation

### 2.3.1 120 GHz Radar

For above 100 GHz band, Chalmers will provide 120-123 GHz single channel FMCW radar evaluation platform for localization tests. The hardware is from SiliconRadar company and detection software are developed by chalmers using Matlab and Python. The hardware is shown in Figure 2-7.

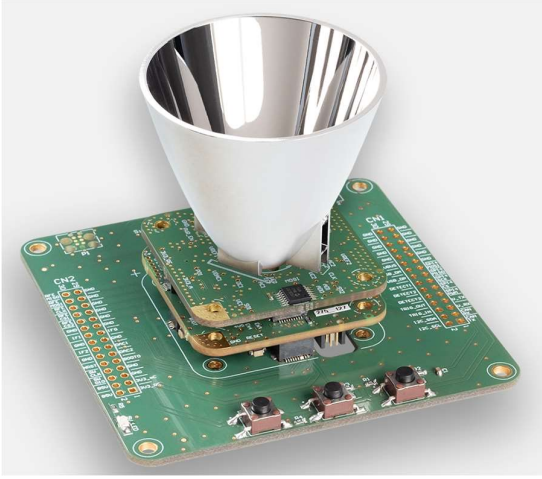

**Figure 2-7. 120 GHz Radar Evaluation Platform**

### 2.3.2 77 GHz Radar

Chalmers also modified 77 GHz radar hardware from Texas Instrument to fit with extra high gain antennas for enhanced detection range. This platform can be used as multiple channel MIMO FMCW radar, detection algorithm is developed by chalmers based on Matlab, the hardware picture is shown in Figure 2-8.

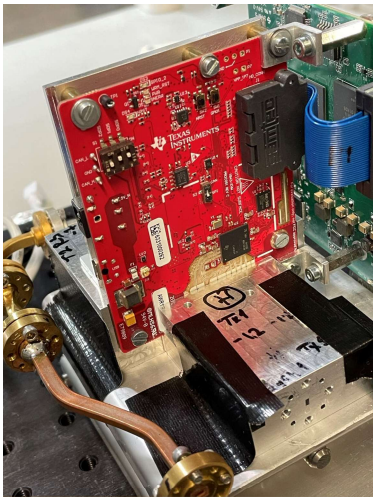

**Figure 2-8. 120 GHz Radar Evaluation Platform**

### 2.3.3 Mechanical Movement Arm

Chalmers will provide 2.3 meter digital controlled mechanical movable arm which also equipped with rotational platforms. The movement can be programmable controlled with 10um movement accuracy and 0.1 degree rotation step as shown in Figure 2-9.

**Figure 2-9. Programmable movement arm for accurate localization characteristic**

Keysight PNA-X Network Analyser with VDI extender can be configured as radar test setup which covers from 50 GHz to 1.7 THz. Figure 2-10 shows a setup of PNA-X based gated radar test at 240 GHz band.

**Figure 2-10. Programmable movement arm for accurate localization characteristic**

# 3 RIS Hardware Description

## 3.1 GW RIS Prototypes

Greenerwave has already developed a RIS (GW-3) operating in the Ka Tx band (27-31 GHz) as depicted in Figure 3-1. The RIS size is 200x200 mm. The RIS is controlled by MATLAB or Python software and is capable to operate in the Far-to-Far field and Near-to-Far field regime. The RIS reflects the electromagnetic signal and is capable to perform single or several beams with controllable beam direction, frequency, polarization, and beamwidth. The beam switching rate reaches hundreds of milliseconds.
The RIS is inherently passive structure and has a very low power consumption (few Watts in the idle mode and 18 W average in operational mode). The RIS has a low RF dissipation level below 2.5 dB in reflection. The RIS has an industry ready design and can be rapidly fabricated in a required number of samples.

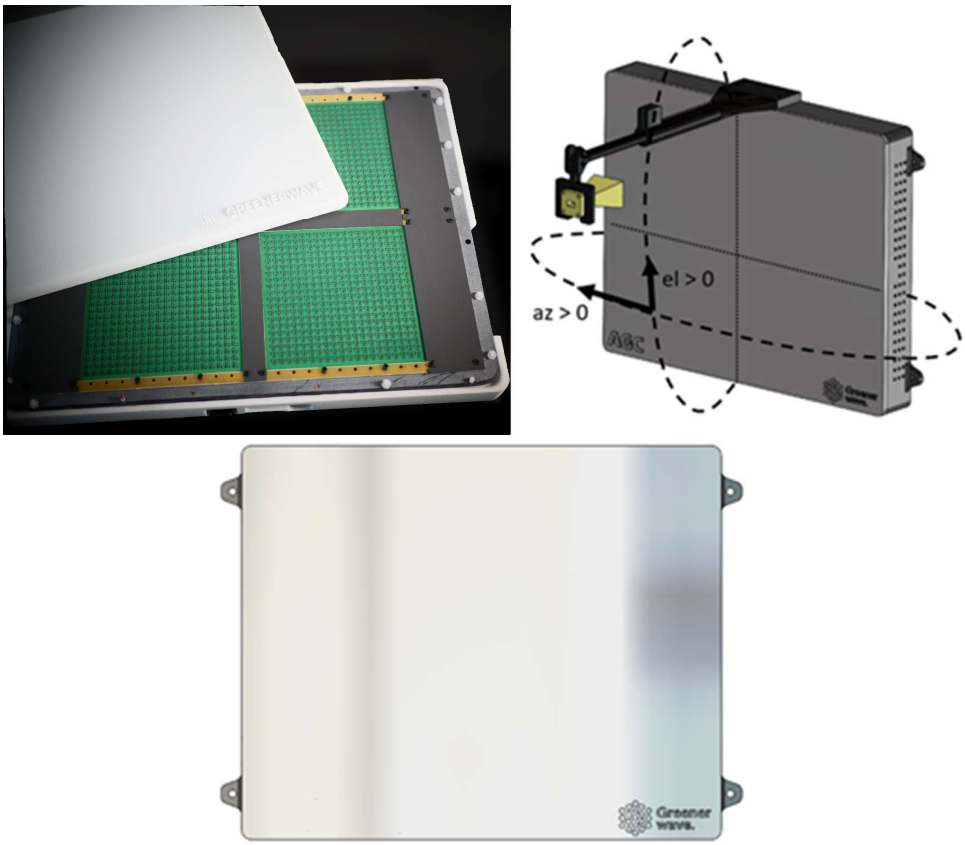


**Figure 3-1. Greenerwave's RIS view: a) front b) perspective**

RIS specifications are provided in Table 3.1.

**Table 3.1. Greenerwave's RIS specification**

| | |
|---|---|
| *Supply Voltage* | 5VDC/200mA (USB), 12V/4.5-5A Barrel Jack 5.5mm/2.5mm |
| *Operating Temperature(ambient)* | 5 ~ 40 °C |

| | |
|---|---|
| *Active RIS surface* | 200 mm * 200 mm |
| *Outline case dimension* | 350 mm * 260 mm * 40 mm |
| *Weight* | 1.6 kg |
| *Type of USB connector* | micro USB |
| *Power Consumption* | ave. 20W, max 40W, min 2W |

| | |
|---|---|
| *Freq. range of operation* | 27.0-31.0GHz |
| *Instantaneous bandwidth* | 500 MHz |
| *Polarization* | dual, H-pol and V-pol |
| *Half power beam width* | 3-5 degree |
| *Scan Range (Azimuth, Elevation)* | +/- 60 deg. |
| *RF Power Handling* | max 50W |

| | |
|---|---|
| *Software OS* | Windows10 and Ubuntu(Linux) |
| *Program language* | Python 3.8.x |

## 3.2 CEA RIS Prototype

CEA-Leti has yet developed two different prototypes: one switchable dual circularly-polarized T-RIS operating in the frequency band 27 – 31 GHz and a vertical linearly polarized T-RIS operating in the band 24 – 32 GHz. The two T-RISs, with a radiating aperture equal to 100×100 mm², are composed of a square array of 20×20 unit cells integrating on the radiating elements two p-i-n diodes. By controlling the bias current of the 800 p-i-n diodes in the range ±1 – 10 mA, it is possible to electronically program the phase distribution on the T-RIS aperture and control the transmitted electromagnetic filed. A 1-bit phase distribution, each unit cell has a phase shift of 0° or 180°, is generated at the aperture to simplify the design, have a relatively low cost, and reduce the power consumption (5 W when a current of 5 mA is used as bias).

Both T-RIS prototypes are controlled considering a specific electronic board connected by a USB link to a computer **Erreur ! Source du renvoi introuvable.** 3.2(a)). A specific C+/MATLAB program has been also developed to load the required phase distribution (**Erreur ! Source du renvoi introuvable.** 3.2 (b)). The MATLAB code is also used to calculate the phase distributions to generate a specific radiation pattern, e.g. beam steering, beam splitting, focalization in the near- and far-field regions. To validate the propose design a board emulating the T-RIS (**Erreur ! Source du renvoi introuvable.** 3.2 (c)), which integrates led-based diodes, has been designed and fabricated.

To validate the radiation performances of the proposed T-RISs, they have been experimentally characterized in the CEA-Leti far-field antenna facility (**Erreur ! Source du renvoi introuvable.**(a)). The T-RISs have been illuminated by a standard gain horn having 10 dBi of average gain on the operation frequency. The horn is located at a distance of 60 mm from the array aperture. The phase distributions required to collimate the radiation pattern in different direction up to ±60° have been computed and used to steer the beam. As results, an electronically beam-steering has been successfully demonstrated.

The measured co-polar radiation patterns computed on the H-plane and the gain frequency response at broadside (beam collimated at 0°) have been presented in (**Erreur ! Source du renvoi introuvable.**(b)-(e)). A peak gain higher than 20 and 23 dBi has been demonstrated in the case of the circularly- and linearly-polarized T-RISs, respectively.

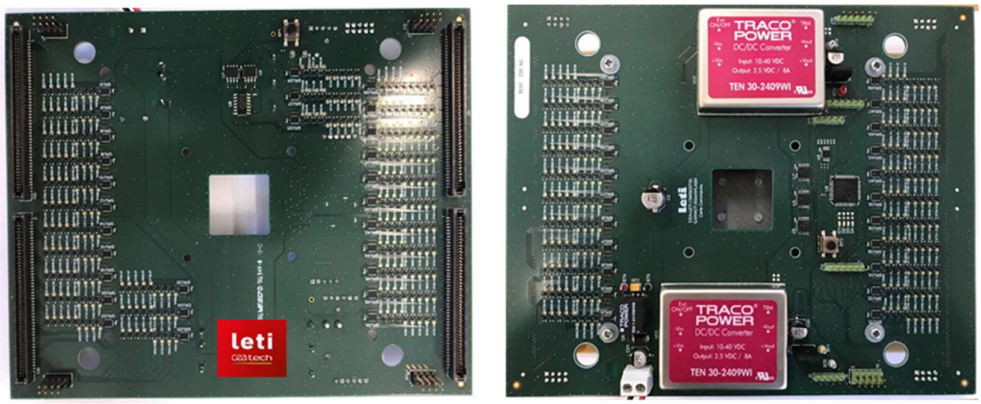


**Figure 3-2. Photograph T-RISs control board (top and bottom layers), respectively**

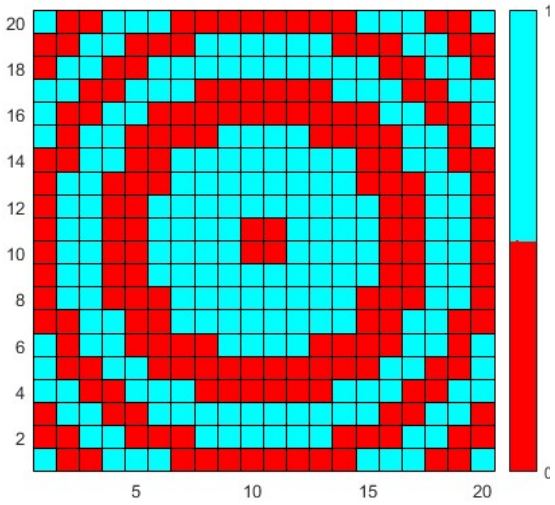


**Figure 3-3. Example of a 1-bit phase distribution of the T-RIS computed with the CEA-Leti program**

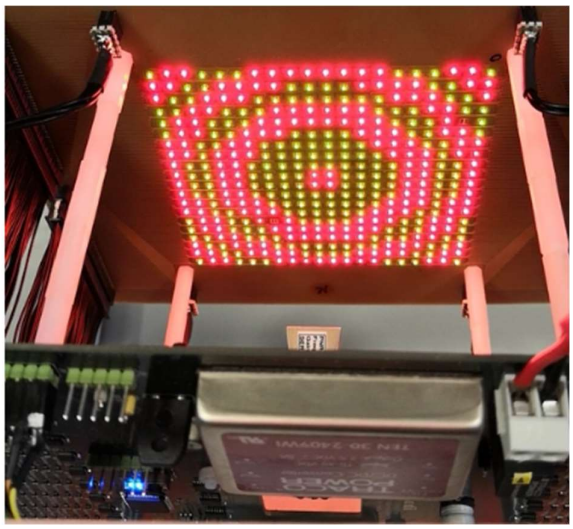

**Figure 3-4. Test of the electric control board using LED diodes**

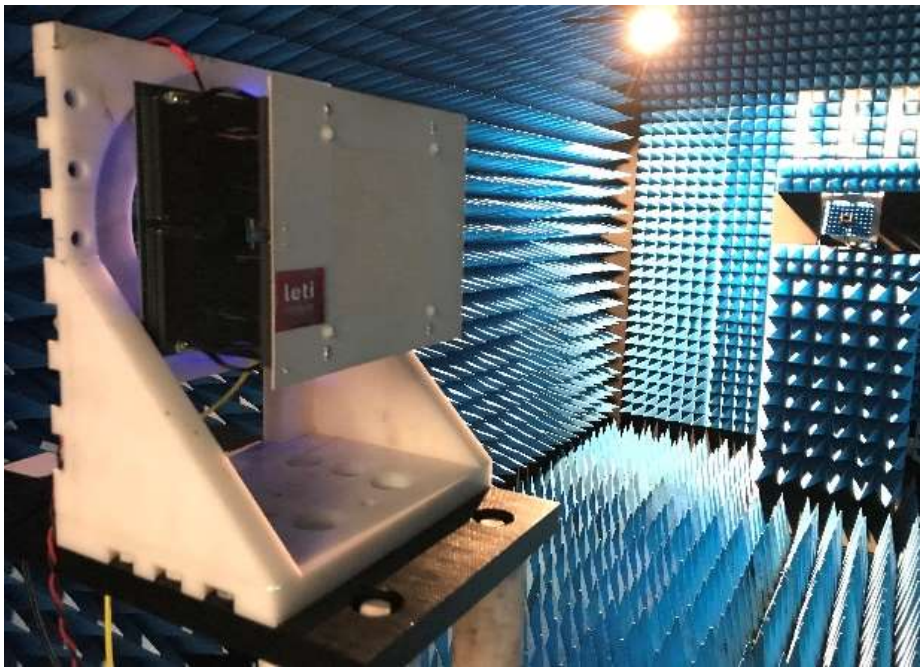


(a)

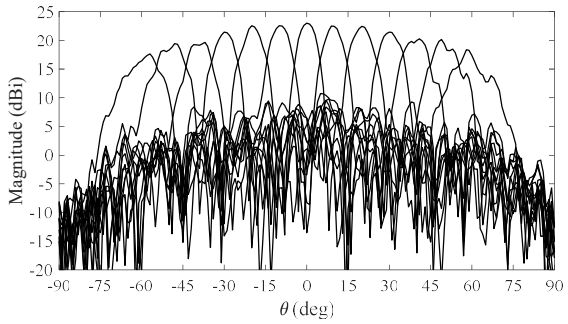


(b)

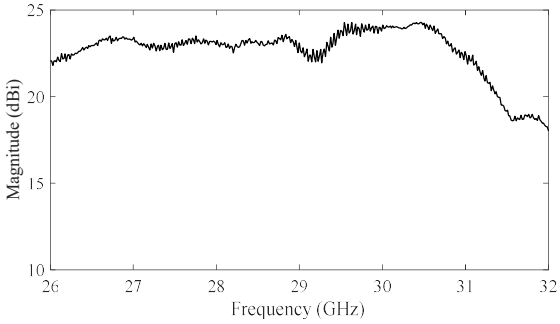


(c)

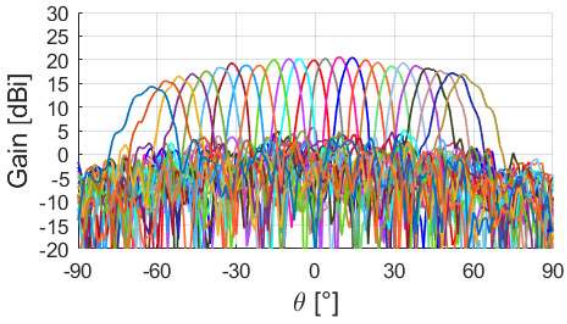


(d)

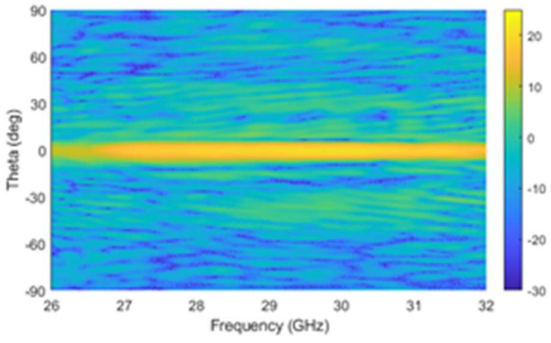


(e)

**Figure 3-5. (a) Figure 3-5. Photograph of the T-RIS developed at CEA-Leti during the measurement campaign in anechoic chamber. Measured radiation patterns as a function of the scan angle (±60°) at 29 GHz of the linearly-polarized, (b) and circularly-polarized (d) T-RISs, respectively. Measured frequency response of the linearly-polarized (c) and circularly-polarized (e) T-RISs, respectively.**

## 3.3 AAU RIS Prototype

The AAU RIS design consists of dual-polarized patch elements partitioned into segments with 4x4 patches sharing a control board. Partitioning allows for higher flexibility during production, and allows for experimenting with spacing between the elements. The final RIS array will consist of 2x2 or 4x4 arrays of these segments, resulting in 8x8 or 16x16 experimental configuration. The patch scatterers are designed to operate in the 3.6–3.8 GHz band.

Detail of the patch scattering element used as a unit cell in the CST simulations is shown in Figure 3-6. To improve on efficiency, the patch is printed on the back side of suspended low-loss F4BM substrate (not shown), so that there is an air gap between the patch and the ground plane. The ground plane is on the front side of a FR-4 substrate whereas the two RIS loads, one for each polarization, are placed on its back.

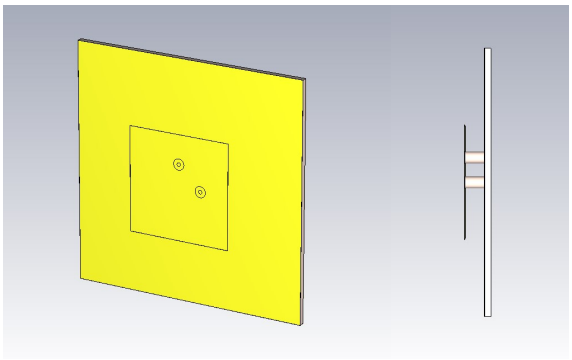

**Figure 3-6. Detail of the array element unit cell; circles show the feeding points of the patch**

The array has been modeled in CST Microwave Studio using the unit cell approach in two directions and tetrahedral mesh F-solver. The unit cell is excited by an incident wave from the front while the reflection coefficient of the load is varied through four points on the outer rim of the Smith chart. Figure 3-7 shows the backscattering/reflection coefficient of the vertical polarization (horizontal has similar properties) magnitude and phase.

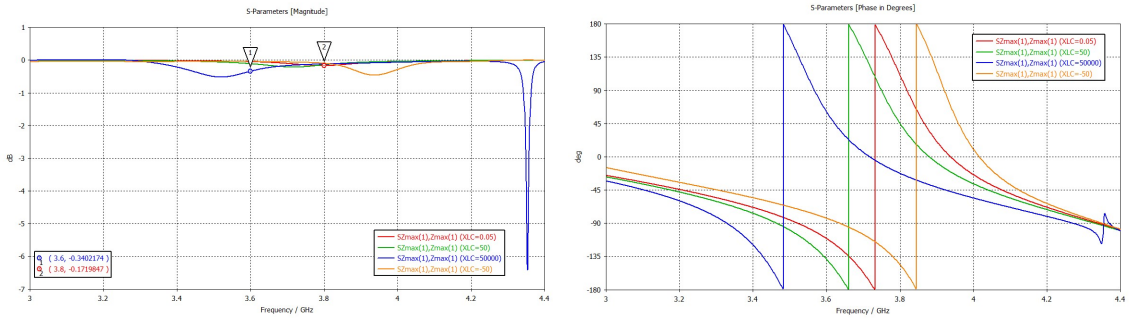


**Figure 3-7. Reflection coefficient magnitude (left) and phase (right) of the boresight incident wave for various loads: red, green, blue and orange stand for the phases {180, 90, 0, -90} of the load reflection coefficient, respectively**

The return loss of the unit cell is within 0.5 dB in the desired frequency range 3.6–3.8 GHz for all preset reflection coefficient values. The phase variation is fastest between 0 and –90 phases of the load reflection coefficient, i.e. in the low capacitance region, however the actual distribution of phases will depend on the selected MEMS components and their matching to the patch feed—this is still work in progress.

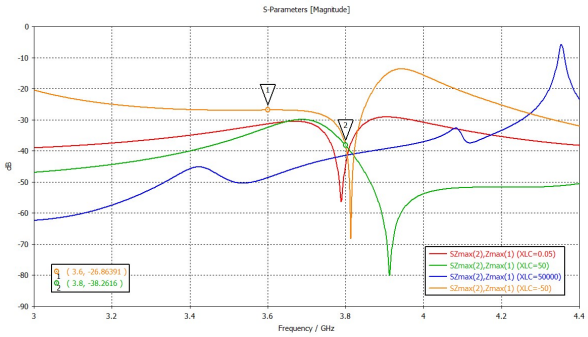


**Figure 3-8. Cross-polarization coupling between boresight incident and reflected waves for various loads: red, green, blue and orange stand for the phases {180, 90, 0, -90} of the load reflection coefficient, respectively.**

The RIS array should also operate independently for both polarizations, which can be seen in Figure 3-8. The cross-polarization of the scattered wave in boresight is below –25 dB in the entire frequency band.

The loads for each polarization will consist of two MEMS capacitors each with 5-bit control range. The control board should be common for the 4x4 building block of the array, with daisy-chaining of all the blocks in the entire array. Preselected values of the capacitors will be stored in a non-volatile memory placed on board, allowing for fast switching via lookup tables.

## 3.4 ORANGE RIS Prototype

### 3.4.1 ORA RIS @ 5.2 GHz

A first ORA RIS previously designed for a reflectarray antenna [RBF13] is working at 5.2 GHz and consists of a controllable High Impedance Surface (HIS) with varactors diodes. The use of varactor allows to control continuously the reflection phase coefficient in a range greater than 300° sufficient to steer the beam in the conical angular of 60° around the normal of the surface.

The 14mmx14mm unit cell as per Figure 3-9 is a “mushroom” cell composed by a metallic patch with a grounded central via. An annular slot divides the printed patch in two parts and 4 varactors diodes are connecting the two parts. The biaising circuit needed to isolate RF signal to DC for applying the inverse voltage to the varactors is designed in printed technology with spiral inductors (RF choke) and grounded surrounded central via (RF short circuit).

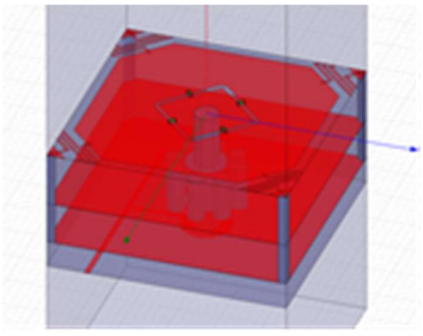

**Figure 3-9. 3D view of the unit cell**

A test coupon of 14x14 controllable unit cells has been manufactured to measure the phase coefficient of the surface to validate the design as shown in Figure 3-10.

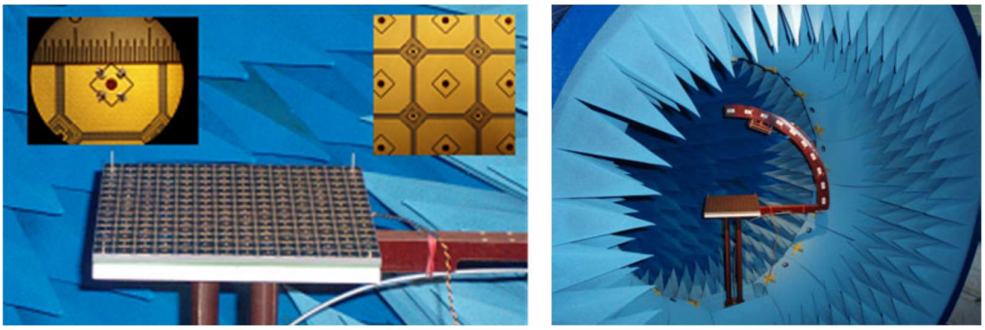

**Figure 3-10. Test coupon with 14x14 unit cells**

In Figure 3-11, the simulated and measured reflection phase coefficients are presented for the 2 polarizations and several incidences of the electromagnetic field. Simulation and experiments are in good agreement and a stable 320° phase excursion for all incidences and polarizations is obtained.

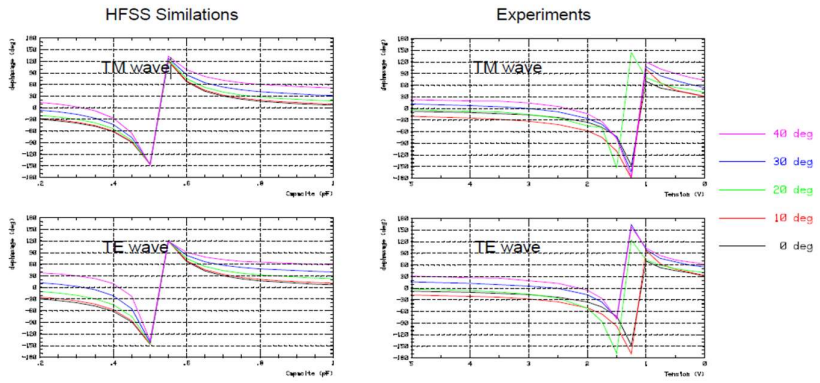


**Figure 3-11. Comparison of the reflection phase coefficients**

Then, a planar reflectarray with a diameter of 503 mm has been manufactured as depicted in Figure 3-12. The 984 unit cells are controlled independently thanks to a control panel placed behind. The inverse voltage is adjusted with a digital potentiometer with 256 steps from 0V to 5V.

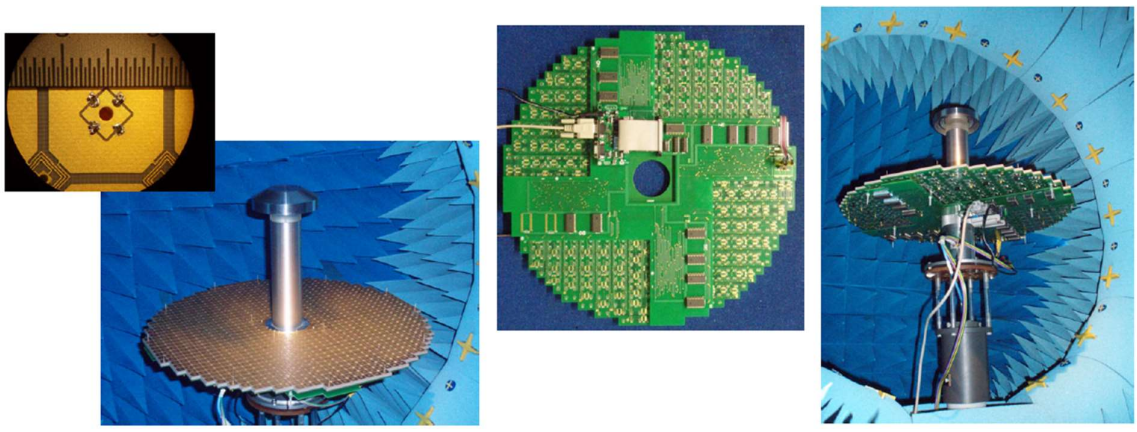

**Figure 3-12. View of the manufactured reflectarray antenna with its control panel**

### 3.4.2 ORA RIS @ 26.0 GHz

A second controllable surface is under designed with the capability to control independently two orthogonal polarizations in the 5G FR2 frequency band 24.25 GHz to 27.50 GHz. As for the 5.2 GHz surface, the controllable surface is based on a HIS including varactor diodes for the phase control.

The selected printed unit cell is based on two orthogonal metallic strips with a central metallic post connected to the ground plane at the center of the intersection. A slot on each arm of the cross is added and the varactor diodes are placed to connect the two parts.

After the parametric analysis of the cell considering a capacitance excursion of the varactor diodes from 20.0 to 200.0 fF, the "RF unit cell" is presented in Figure 3-13. The cell size is fixed to 4mm x 4mm.

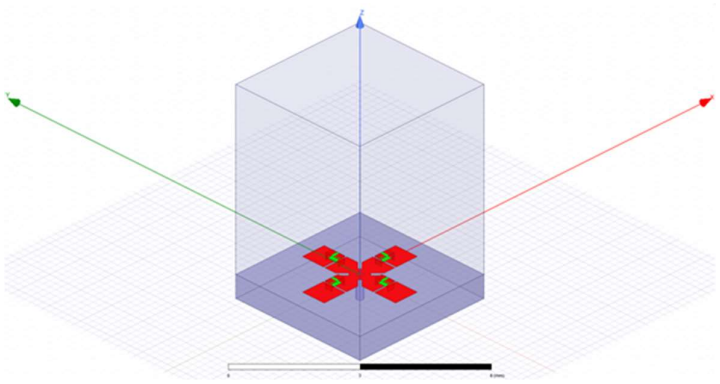

**Figure 3-13. RF unit cell configuration with varactor diodes**

Figure 3-14 presents the reflection phase coefficient of the unit cell in normal incidence for the varactor capacitance varying between 20.0 fF to 200.0 fF at 24.25 GHz (green line), 26.0 GHz (red line) and 27.5 GHz (blue line). At least, 300° of phase control can be expected in the working frequency band.

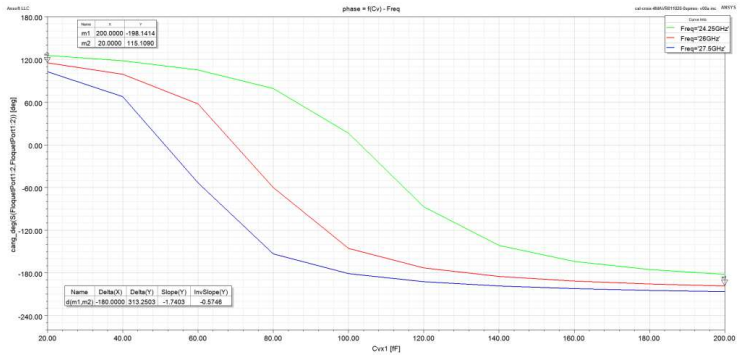


**Figure 3-14. Reflection phase coefficient depending on capacitance excursion at 24.25, 26.0 and 27.5 GHz**

Figure 3-15 and Figure 3-16 present the reflection phase coefficient between 20.0 GHz and 30.0 GHz respectively in normal incidence for several value of capacitances and for a 100.0 fF capacitance value for several incident angles of the EM field. As expected, a 300° phase excursion is observed with a stable behavior depending on the incident angles.

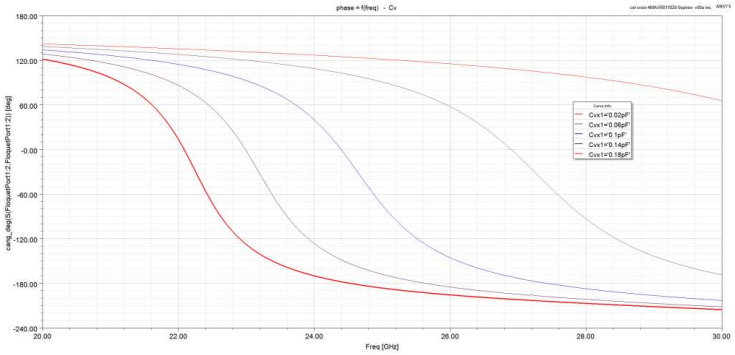


**Figure 3-15. Reflection phase coefficients depending on frequency for several capacitance values**

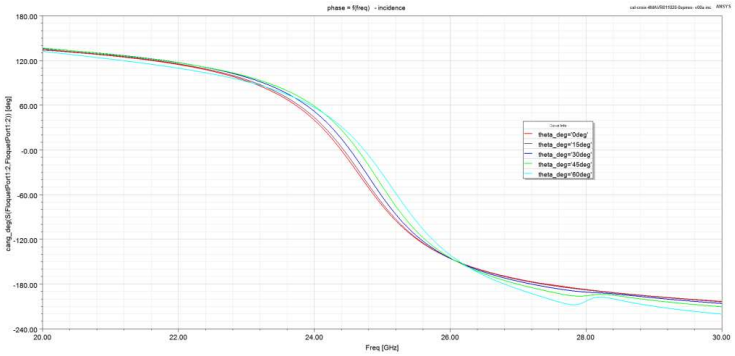


**Figure 3-16. Reflection phase coefficients depending on frequency for several angle of EM field incidence**

As for the 5.2 GHz unit cell, a biasing circuit needs to be included to isolate RF currents to DC currents without discrepancies on the reflection phase coefficient. Printed inductances and capacitances well designed and placed in the biasing circuit are added as shown in Figure 3-17.

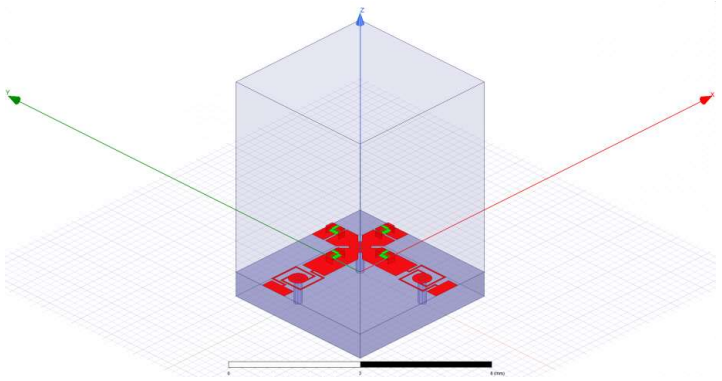

**Figure 3-17. Unit cell including part of the biasing circuit.**

All the components of the unit cell (dielectric substrate, varactors diodes) are under test to have a fine tuning of the design before the manufacturing of the controllable surface. A control panel is under design to be able to control independently the cells of the surface.

## 3.5 Chalmers RIS Prototype

### 3.5.1 Chalmers RIS D-band Prototype

At D-band 110-170 GHz, there are limited commercially available components, therefore the development of RIS includes the activities of integrated circuit design, integrated circuit packaging and RIS array design. Chalmers used 130nm SiGe BiCMOS process provided by Infineon to design the integrated circuits. The overall RIS element IC architecture is shown as figure below.

Each RIS element contains input and output on chip antennae and amplifiers are added at after input antenna and before output antenna to compensate high freespace loss at these frequency bands. A quadrature active mixer core is used to phase shift input signal with vector modulation concept. The quadrature mixer core comprises hybrid phase shift, and power combine network and two mixers controlled by baseband analog IQ signals.

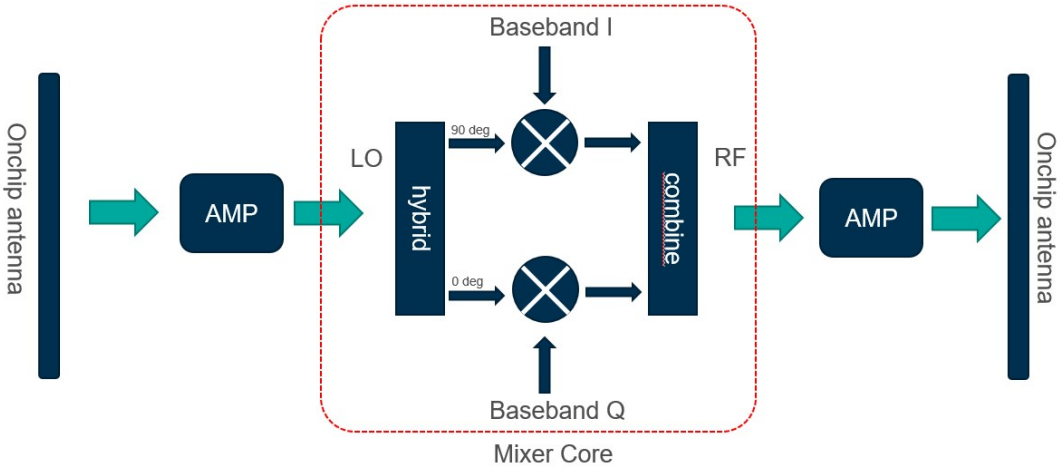


**Figure 3-18. Chalmers Dband RIS hardware IC block diagram**

The designed RIS element IC is 3000um x 730 um in size, with DC bias input on top and differential IQ baseband input PADs at bottom. Antennas are placed at left and right edges. The antenna is designed to have 6 dBi gain at 145 GHz, which requires the IC to be mounted over a customized metal block.
It worth mentioning that the on-chip antenna can also be used transition to a standard waveguide interfacing by changing the metal block design. Conversion to a standard waveguide interfacing allows higher gain antenna to be used for enhancing D-band RIS performance.

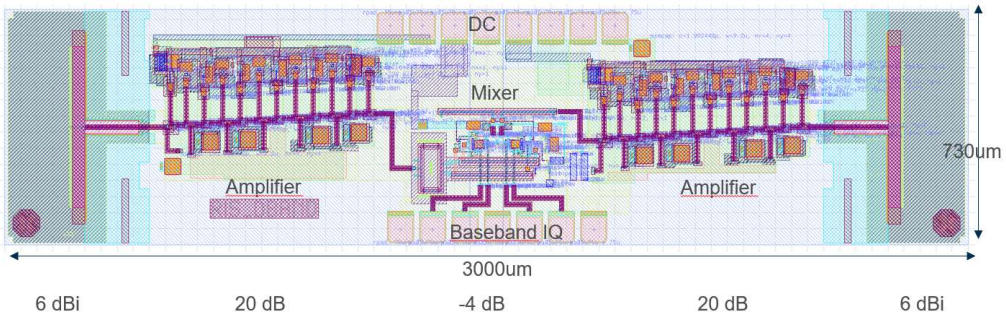


**Figure 3-19. Chalmers Dband RIS hardware IC layout picture**

A separate antenna back-to-back testing IC is design, fabricated and packaged into a customized waveguide split blocks as a test for waveguide interfacing. The test block has two waveguide interfacing to chip transition and the block is tested and result shows averaging 3 dB loss between 130-170 GHz.

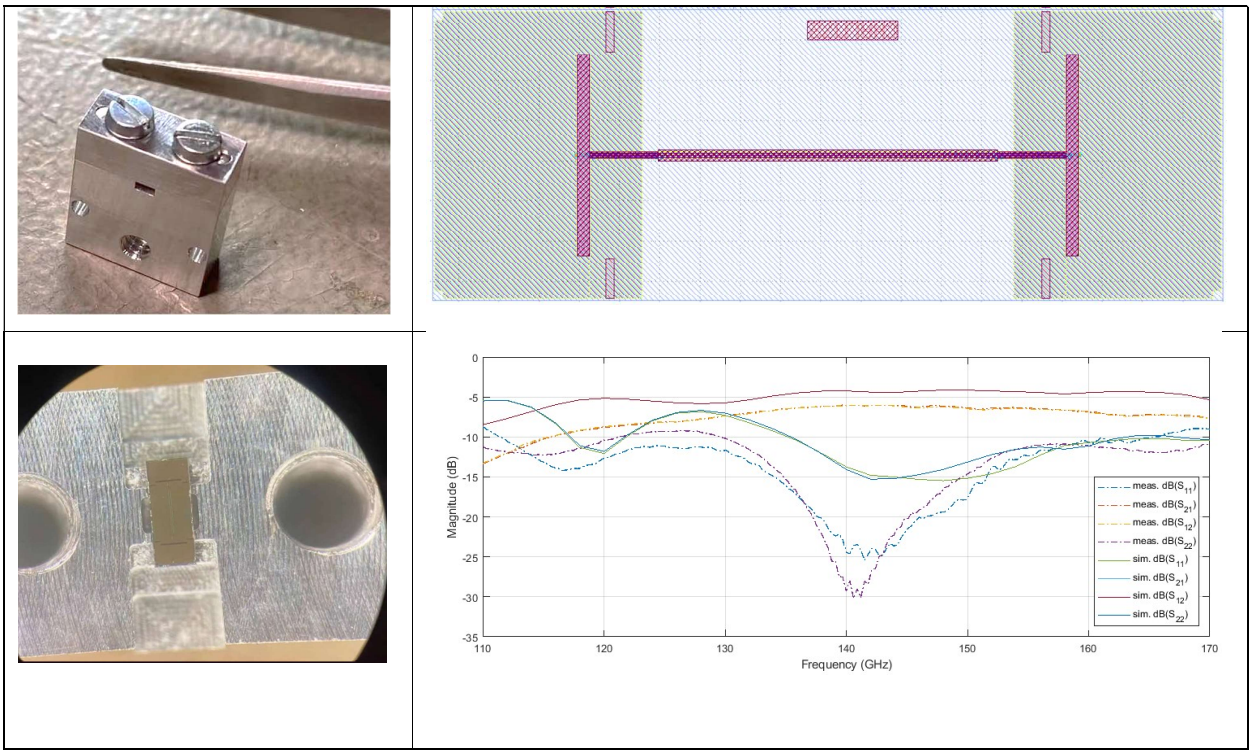


**Figure 3-20. Chalmers Dband RIS antenna validation**

### 3.5.2 Chalmers RIS V-band Prototype

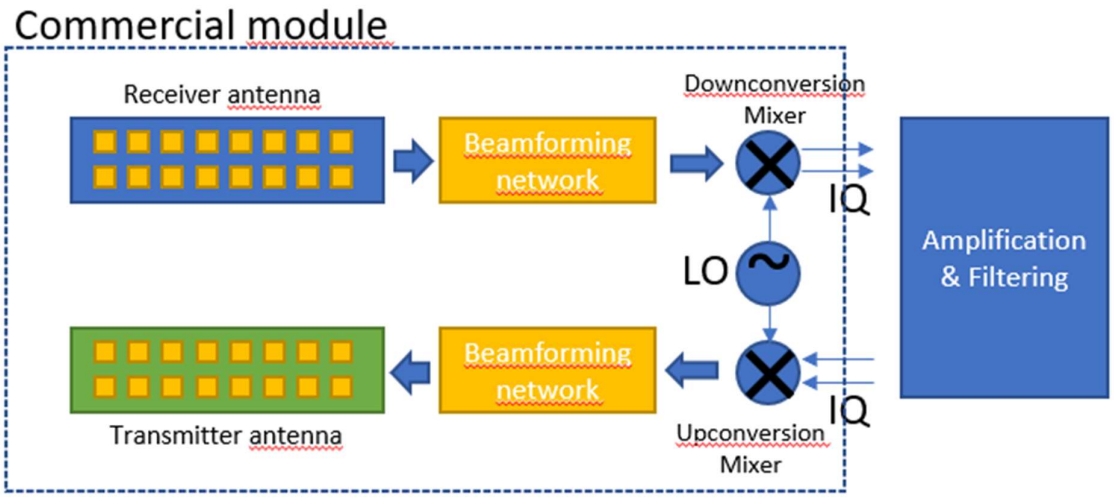


**Figure 3-21. Chalmers Vband RIS based on commercial modules**

SiversIMA's V-band 58-71 GHz transceiver modules are modified as RIS modules. The module contains down-converter and up-converter which share a common local oscillator (LO). When receiving V-band signal, the signal is firstly down-converted to DC-800 MHz differential quadrature baseband signals, and in turn, the baseband signals are filtered and amplified then up convert back using same LO. The result is that the transmission signal has same frequency as incident signal. The receiver antenna and transmission antenna has separate 3x16 array with horizontal beam steering capability, which allowed it to change reflection direction for a controlled RIS steering.

The configuration and controlling of the RIS is achieved with Python code over a USB serial port connected to the siversIMA module. The beam can be steered with 1 degree step within +/- 60 degree range.

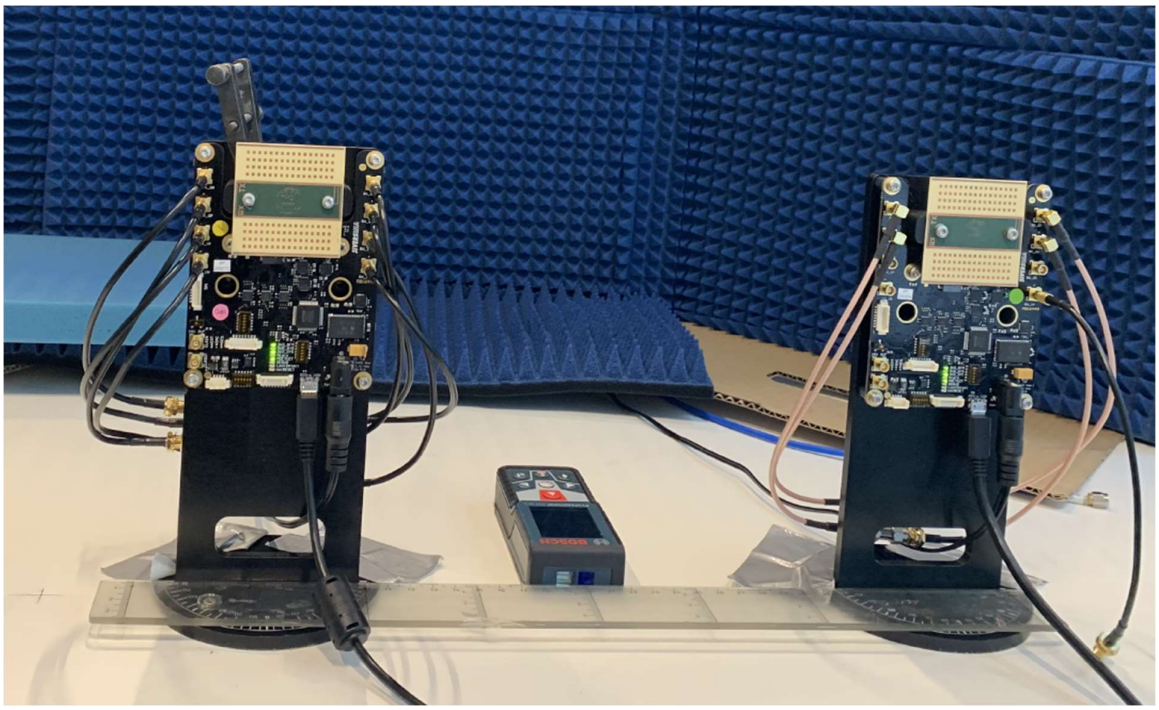

**Figure 3-22. Chalmers Vband RIS antenna validation**

## 3.6 NEC RIS Prototype

The NEC RIS prototype consists in a square with sides of length 272.54 mm and composed of 10x10 unit cells. Each unit cell has dimensions 19.4 x 15.97 mm (right-hand side) and con-sists in a patch antenna, a feeder line, and some associated control logic, which are designed to work at the frequency of 5.3 GHz. The inter-element spacing is fixed at half the operating wavelength. Such value is chosen to strike a trade-off between increasing the number of RIS elements in the same physical space and avoiding unwanted array non-idealities, such as mutual coupling or grating lobes.

The high-level view of the proposed RIS design is shown in Figure 3 23. On the left-hand side, each unit cell is connected to a central MCU via a pair of selection buses, namely the *row* and *column* buses. This design choice allows to scale down the number of connections to the MCU by limiting it to the number of rows plus columns of the RIS (as opposed to one connection per unit cell). Moreover, each unit cell receives its phase-shifting configuration via 3 *phase bus*, whose state is controlled by the MCU. On the right-hand side, the schematic of each unit cell is shown: a patch antenna leads the incoming signal to an RF switch, which in turn is connected to 7 different open-ended delay lines, plus a matched 50 Ω resistor. Each of the latter realizes a specific phase-shift, thus providing this prototype with a 3-bit granularity. Moreover, the matched absorbed is used to effectively turn-off the specific antenna by avoiding signal

reflection back to the antenna. The RF switch configuration is set via 3 FLIP-FLOP, which then load the new configuration from the phase bus whenever the AND gate outputs a high state.
Lastly, the RIS design is such that multiple boards can be connected to create larger structures, while maintaining the half-wavelength separation among antennas.

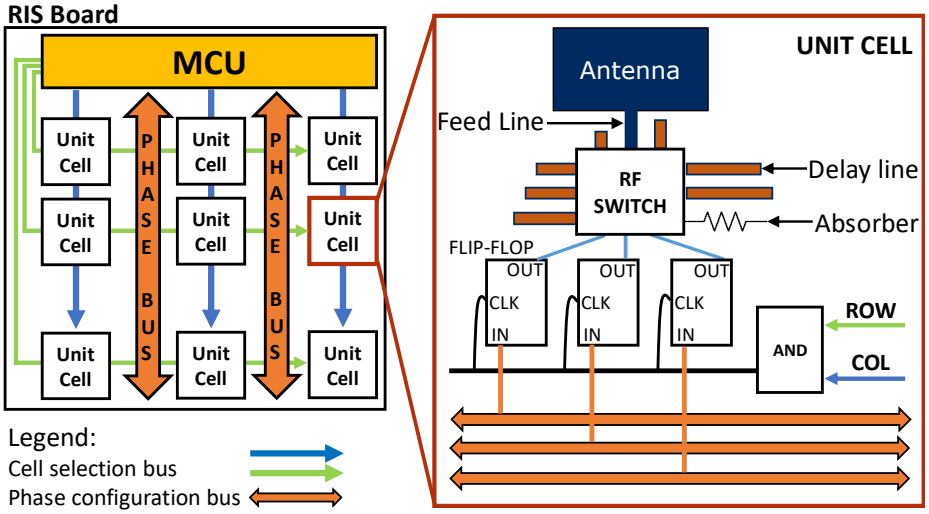


**Figure 3-23. NEC sub-6GHz high-level RIS design (left-hand side) and schematic of each unit cell (right-hand side)**

Each unit cell is designed to operate at 5.3 GHz as shown in Figure 3-24. Here, we compare the full-wave simulation in CST with measurements operated with a VNA. The offset from the theoretical simulation to the experimental measurement is due to an error in the nominal permittivity used in the simulations of the PCB substrate.

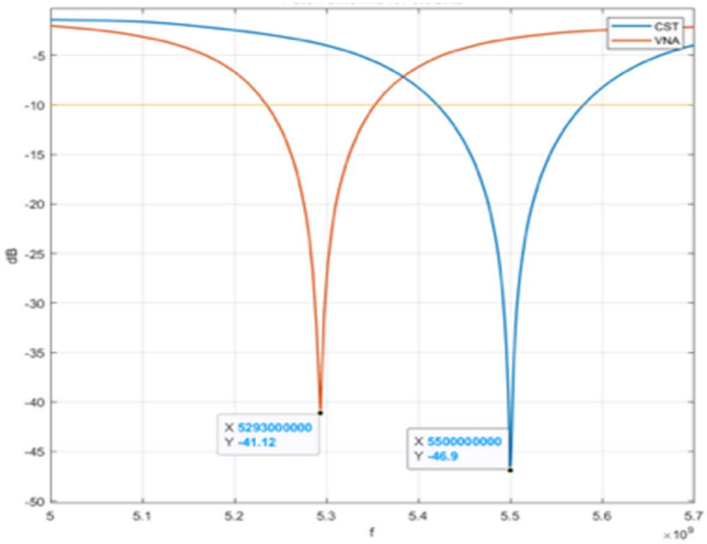


**Figure 3-24: S11 parameter of the NEC RIS unit cell**

The final printout is shown in Figure 3-25.

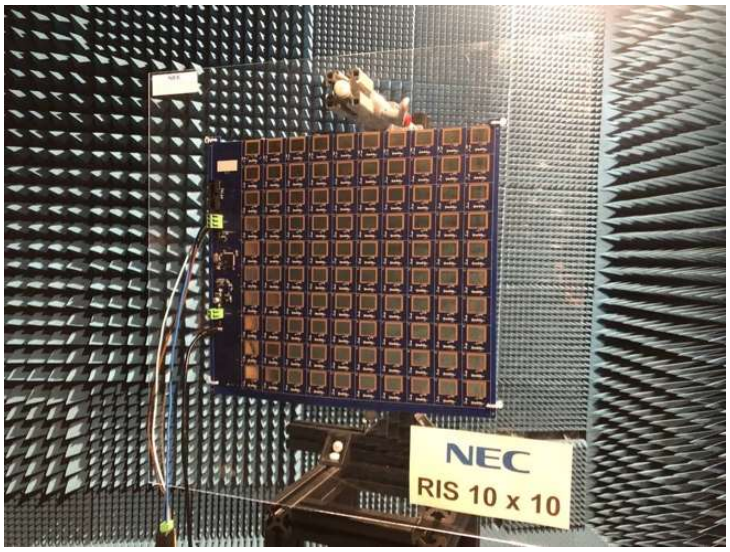


**Figure 3-25: Final PCB printout of NEC RIS prototype**

As depicted in Figure 3-26, experimental validation of the proposed NEC RIS design was conducted in an 8 x 5 m anechoic chamber, where the transmitter, namely a USRP connected to a horn antenna, is placed in the vicinity of the RIS and at a fixed angle. The latter is fixed on a rotating table, which can be remotely controlled. The link between the transmitter and the RIS is fixed at angle $\theta_t$, meaning that they both rotate together with the turntable. A receiver, i.e., a horn antenna connected to a USRP is placed on the other side of the chamber. The latter allows us to verify the received power of the reference transmit signal, not only for different RIS configurations, but also for different angles between RIS and receiver, which is denoted by $\theta_r$.

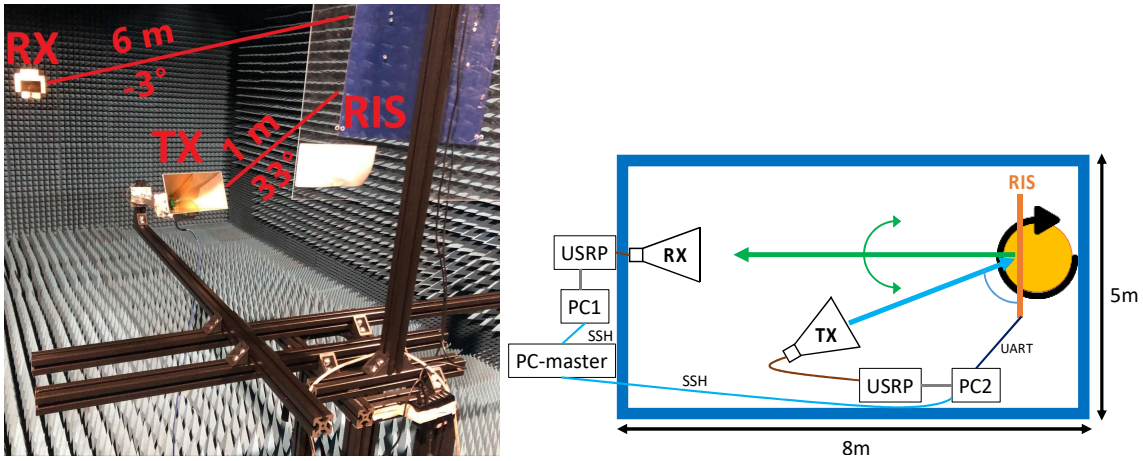


**Figure 3-26: Anechoic chamber measurement setup**

The measured beampatterns are shown in Figure 3-27. Here, the RIS configuration is set to produce a main beam along different directions $(\theta_n, \emptyset_n)$ along the azimuth and elevation, respectively, with $\emptyset_n = -30^\circ$, according to a pre-defined codebook. For every RIS configuration in the codebook, the turntable steers from $-90^\circ$ to $90^\circ$. On the right-hand side, the transmitter-RIS link was fixed to $\theta_t = 90^\circ$, while it was $\theta_t = 20^\circ$ on the right-hand side.

All such results, including details of the RIS prototype, are presented in [RMG+22].

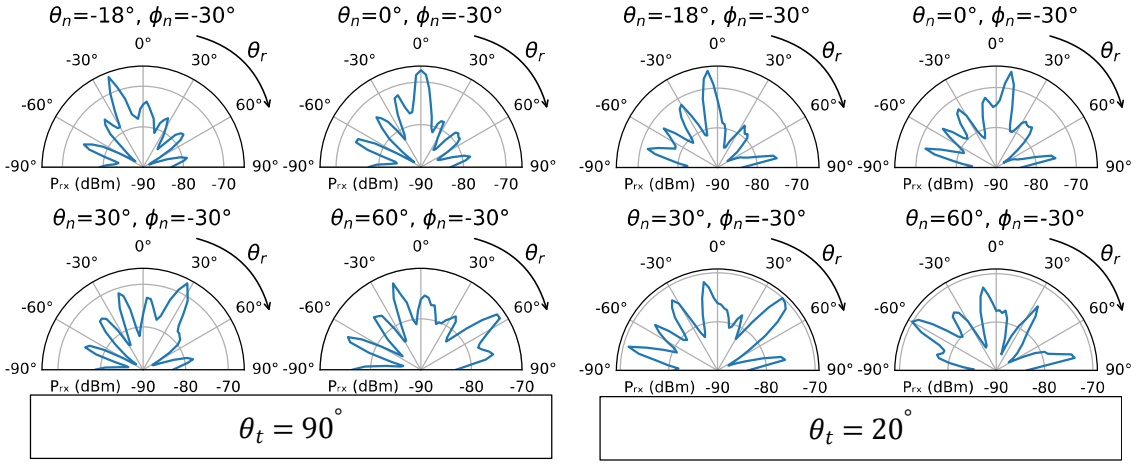


**Figure 3-27: Measured NEC RIS beampattern for different values of $\theta_n$, with $\theta_t = 90^\circ$ (left-hand side) and $\theta_t = 20^\circ$ (right-hand side)**

# 4 RIS Hardware Integration for Communication use-case

We illustrate communication PoC setups, discuss required hardware, instruments (UE, Base station, control link etc) and KPI, i.e., communication throughput, length, steer angle, ect. We will also shed the light on the dependency of setup, indoor room layout, max hope length etc, type of supported UE, standard frequency band etc. Finally, we connect KPI limitation with RIS HW design challenges and add overall power consumption as system level parameters.

## 4.1 GW RIS Prototype Test for Communication

Software-defined-radio (SDR) is an extremely flexible FPGA-based hardware platform that, in conjunction with GNURadio (open-source software platform), allows one to implement various communication schemes. Together with up-, down-converters and local oscillators, a SDR can be used in the following scenarios for different proof-of-concept experimental demonstrations at mmWaves:

- Non-line-of-sight (NLO) RIS-assisted communication (see a schematic below);
- User equipment tracking with RIS;
- Point-to-point communication between two antennas: an electronically scanned array as Rx or Tx and a fixed antenna as Tx or Rx;
- Receiver or transmitter tracking with an electronically scanned array.

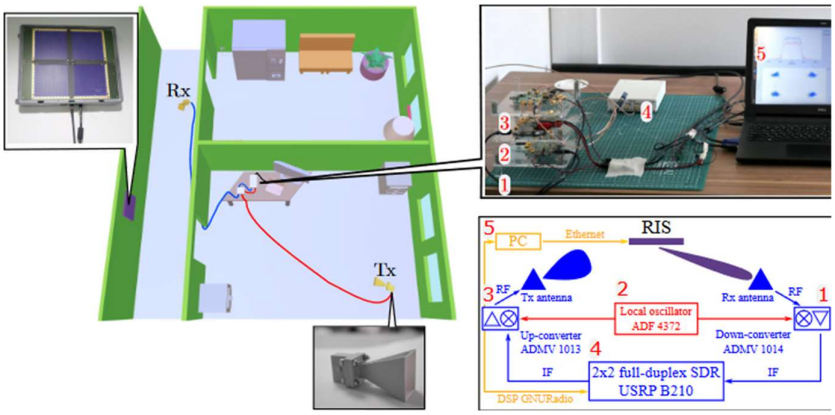


**Figure 4-1. Left: A 3D illustration of the experimental setup used to demonstrate RIS-aided indoor wireless communication in a NLOS situation. Right: A photography (top panel) and a schematic (bottom panel) of the communication module represented by a down-converter 1, a local oscillator 2, an up-converter 3, a SDR 4, a PC 5.**

At mmWaves a signal from a base station experiences significant fading due to propagation loss and shadowing by buildings, landscape or indoor walls. This problem can be solved by installing additional base stations or access point extenders (passive or active) between existing base stations. In this section we demonstrate experimentally the integration of our RIS in an indoor wireless communication system. This experiment shows a great potential of RIS to provide a robust broadband connectivity even in NLOS situations.

To demonstrate operation of the RIS as a passive access point extender we set up an indoor wireless communication system as illustrated by Figure 4-1**.** Here the RIS is placed on a wall of a corridor connecting offices. The Rx and Tx are WR-34 Pyramidal Horn Antennas (Rx) emulating correspondingly an end user terminal (i.e., mobile phone or laptop) and a 5G base station antenna. We start by using a Rohde & Schwartz ZVA40 vector network analyzer (VNA) to characterize the channel when the RIS is put in a beamforming configuration or is switched off. In the beamforming configuration the RIS creates a Line-

Of-Sight (LOS) between the Tx and Rx antennas. However, in order to efficiently redirect the wave radiated by the Tx antenna towards the Rx antenna, it is necessary to know their precise positions with respect to the RIS. In the given experimental setup we first estimate these locations approximately and then use a feedback from the VNA ($S_{21}$ parameter) to scan the space in the vicinity of the estimated location antenna positions. In the scanning procedure the RIS is configured according to estimated positions of the Rx and Tx antennas at given iteration. These positions are used as input parameters for our beamforming algorithm. When the $S_{21}$ parameter is maximized, precise positions of the Tx and Rx antennas are found and the RIS redirects the wave radiated by the Tx antenna towards the Rx antenna establishing the LOS. With a feedback from the base station or the SDR set-up on the quality of the channel, the beamforming algorithm can even be implemented without any channel sounding with VNA. Figure 4-2A compares the path-loss (measured with the VNA) between the Tx and Rx antennas, when the RIS is switched off (the blue curve) and when the RIS is on creating the LOS (the orange curve). It is seen that the RIS allows one to increase the signal power by 30 dB and maintain it at almost constant level in a wide frequency range. The instantaneous bandwidth constitutes more than 3GHz with respect to 29.5 GHz central frequency. On the other hand, when the RIS is switched off the signal level drops below the noise level at 29.5GHz and significantly varies with respect to the frequency.

After the channel is characterized, the VNA is substituted by a wireless communication system shown in Figure 4-1 on the right panels. Unfortunately, we did not have an access to a real base station and had to built our own setup. In this setup a full duplex software-defined-radio USRP B210 by Ettus Research (SDR) is used in the communication system as a transmitter and a receiver of a modulated signal at an intermediate frequency (IF). The SDR generates a waveform at IF in the Tx channel and provides in-phase and quadrature-phase (IQ) received signal in the digital baseband for further signal processing. The RF front- end of the communication system is represented by an up- converter, a down-converter and a local oscillator (LO) by Analog Devices (ADMV 1013, ADMV 1014 and ADF 4372, respectively). Up- and down-converters multiply the LO frequency by four. A PC controls the RIS via an Ethernet interface and performs digital baseband signal processing of the signal received by the SDR. The signal processing is done with the help of an open software platform GNURadio. A photography of the setup and its schematic are shown on the top right of Figure 4-1.

To transmit at the RF frequency of 29.5 GHz, the LO is set at 7 GHz and IF generated by the SDR is set to 1.5 GHz. As a data stream was chosen a large array of random numbers, QPSK modulation followed by root-raised-cosine (RRC) filter creates the transmitted waveform. On the receiver chain, the signal received by the SDR is first put through the same RRC filter, after that timing recovery, equalization and compensation for phase and frequency offset is performed. Finally, the received signal is demodulated. It is important to note that even though the Tx and Rx chain of the SDR uses the same clock, one should compensate for the possible frequency offset after the up- and down- conversion processes.

Figure 4-2B shows normalized power of the received signal at the digital baseband, when the RIS is switched off (the blue curve) and when the RIS is put in the beamforming configuration (the orange curve) to redirect the impinging wave from the Tx antenna towards the Rx antenna. The beamforming by the RIS allows one to enhance the level of the received signal by more than 25 dB and the four symbols of the QPSK modulation are well-distinguished. When the RIS is off, the receiver cannot even lock the constellation as demonstrated by Figure 4-2C-D

Those results clearly demonstrate how Greenerwave RIS allows one to restore a data transmission between two antennas in the NLOS situation and establish a solid mmWave communication channel in a complex indoor environment. Furthermore, additional functionality can be added, when a single base station can serve multiple users simultaneously with the help of a RIS. In this case frequency division,

code division or time division multiple access techniques can be used.

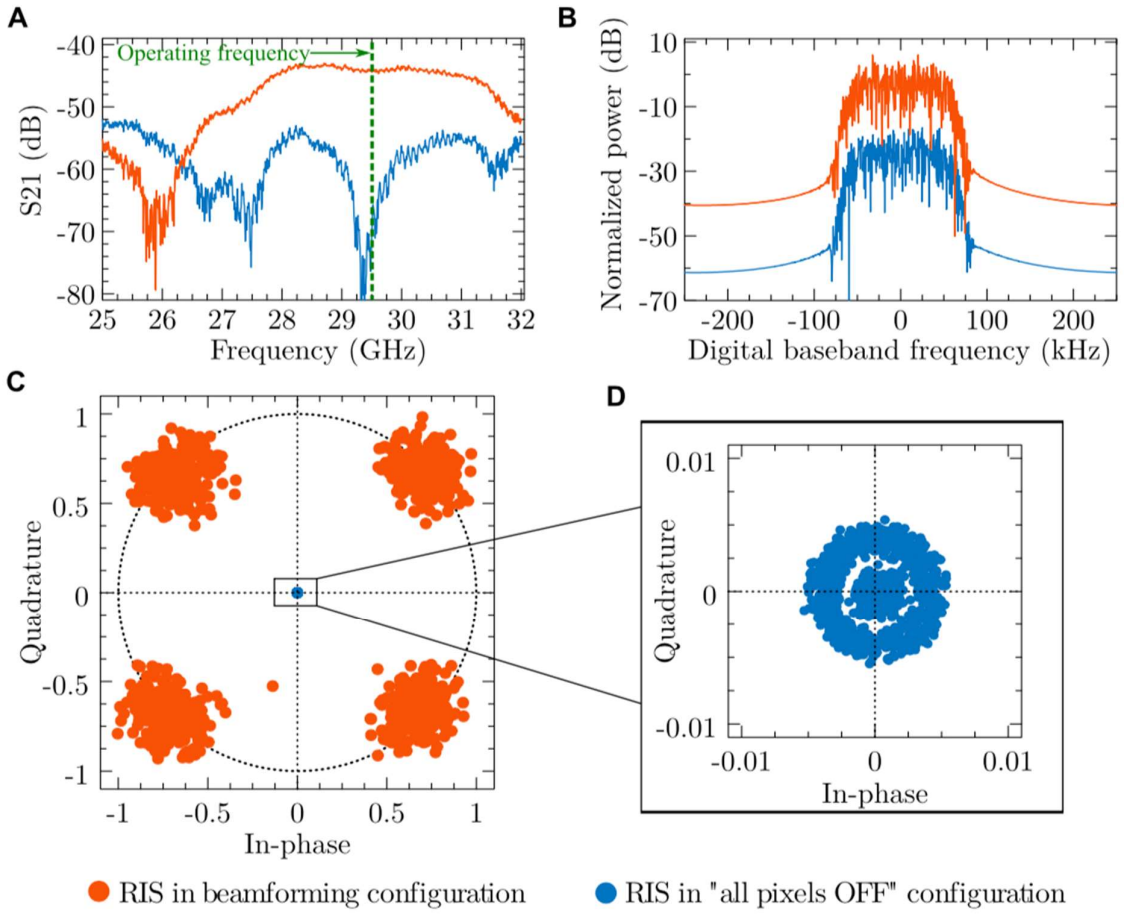


**Figure 4-2. (A) S21 parameter measured with a VNA for channel characterization in two configurations of the RIS: all pixels off and beamforming configuration. (B) The signal received by the SDR and put through an RRC filter, when the RIS is off and on. (C) Constellation diagram after timing recovery, equalization and phase and frequency offset compensation, when the RIS is off and on. (D) Close-up of the constellation diagram when the RIS is off.**

## 4.2 AAU RIS Prototype Test for Communication

The prototype described in this section is overall tested in two different ways, as described in this section.

### 4.2.1 Test of unit cell

The unit cell is configurable by controlling two MEMS capacitors, where each of them can be set to 32 different values for a total of 1024 possible configurations. The first set of tests aims at

- Verifying that the control circuits are working as designed;
- For each configuration, comparing the measured phase and amplitude with corresponding values obtained in simulations;
- Allowing identification of subsets of the total of 1024 settings that result in an acceptable coverage of the 360º phase range for $S_{11}$.

As illustrated in Figure 4-3, the test will be performed in a setup with the unit cell placed in front of a horn antenna / open waveguide, both placed in an anechoic room. The aim is to only illuminate the unit cell, thereby maximizing the impact of the cell for different settings. The received signal will be composed of the signal reflected by the ground plane and the signal due to the patch element. The challenge is to obtain a sufficiently large signal caused by the patch element, compared to the ground plane reflection. A first attempt will be to use a network analyzer to measure $S_{11}$ at a close distance, but it may prove necessary to experiment with other setups such as using a separate offset Tx antenna. For these tests a modified version of the basic RIS module (see Section 4.3) is used, comprising only a single unit cell.

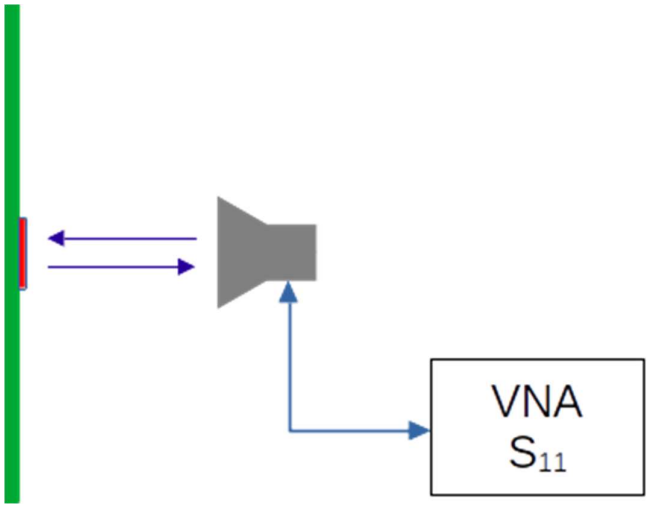


**Figure 4-3. Setup for testing reflection from unit-cell**

### 4.2.2 Test of beam patterns

The overall purpose of these measurements is to verify that beams can be formed by setting the capacitors of each unit cell so that the appropriate phase is achieved. The test is illustrated in Figure 4-4, where it is noted that the figure is only a principal sketch where, e.g., amplifiers may be needed and distances are not to scale.

A fixed Tx antenna is illuminating the RIS from a configurable direction, and the radiation pattern is obtained by $S_{21}$ measurements with the Rx antenna at different angles. A key issue is that far-field conditions may be difficult to achieve, due to the relatively large RIS (about 1.2m) compared to the wavelength. Therefore, the first pattern measurements will be carried out on a sub-set of the RIS, so that beamforming capabilities can be demonstrated in far-field conditions. More advanced measurements may involve AAU's special anechoic room that has the capability to remove one wall and the roof, so that the anechoic room is open to the sky. This allows a large separation between the Tx antenna and the RIS.

Although far-field conditions are desirable from a characterization point of view, real world applications may also involve situations where near-field conditions apply, e.g., when mobile users are close to the RIS. Hence, measurements of the RIS in such conditions may also be studied.

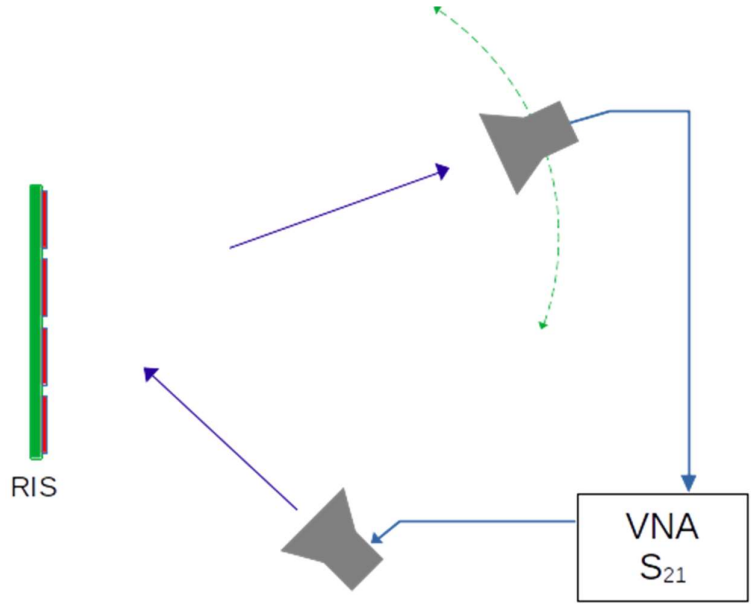


**Figure 4-4: Sketch of setup for measuring the radiation patterns of the RIS**

# 5 RIS Hardware Integration for Localization use-case

Hereafter, we illustrate localization PoC setup, discuss required hardware, instruments (UE, Base station, control link) and KPIs such as localization accuracy, coverage, etc. We analyze the dependency of the setup, indoor room layout, type of supported UE, standard frequency band etc. Finally, we connect setup KPI limitations with RIS HW design challenges and add the overall power consumption as system level parameter.

## 5.1 CHALMERS RIS prototype

Two Chalmers V-band RIS Porotypes are used in a SISO localization experiment to validate localization accuracy at 60 GHz. Two RIS units are deployed at fixed positions under the radiation of a base-station (BS) and reflected the signal in a controlled manner towards a user equipment (UE). The BS and UE are implemented with two VDI V-band extenders with a PNA-X vector network analyser. In this setup the signal loss transmitted by BS to the UE can be measured across a bandwidth of 57-71 GHz with a stepped frequency signal.

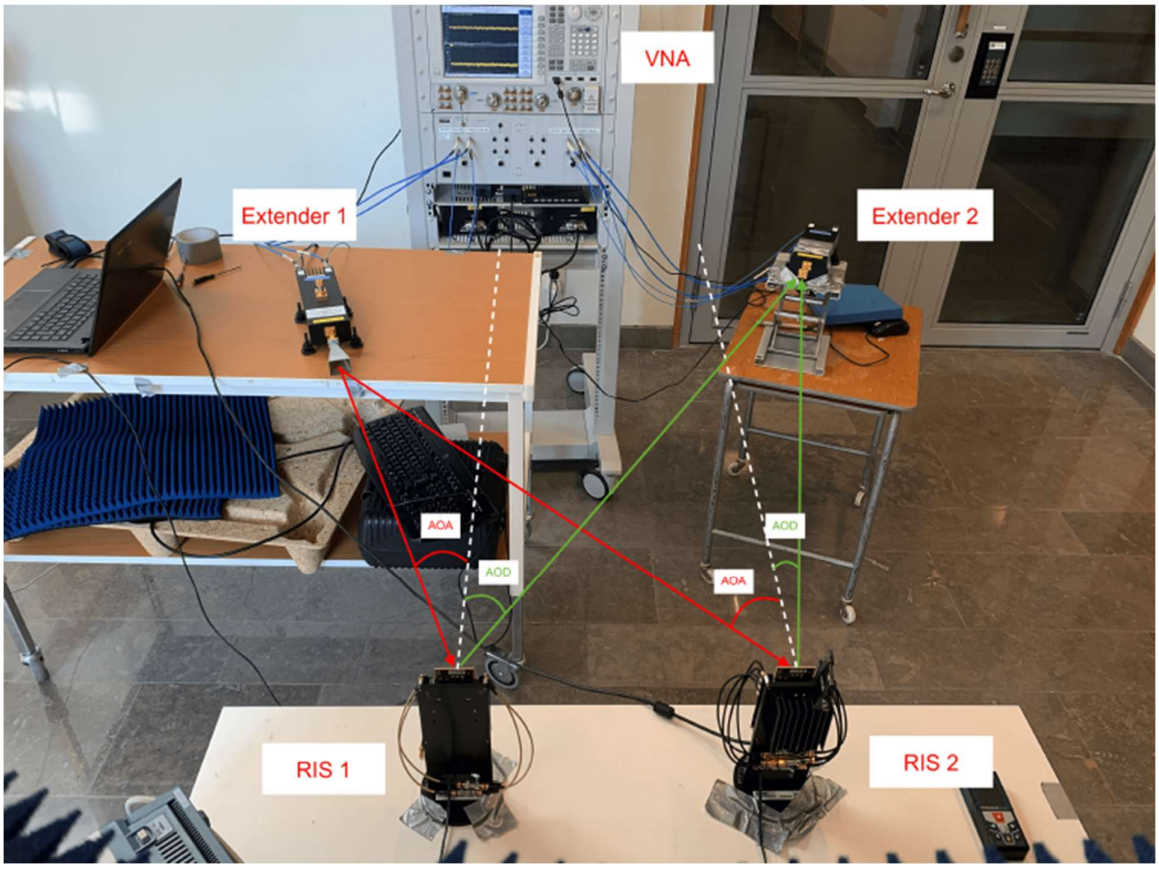


**Figure 5-1. Chalmers Vband localization validation setup**

During the test, the RIS1 and RIS2 reflection beam is steered in horizontal plane. The steering of each RIS beam is independent and the angle is referenced to the centreline of each RIS unit. To perform localization in 2D, each of the two RISs iteratively sets 63 beampattern configurations, which generate different azimuth AoDs. The estimation of the AoDs at the UE side is performed by selecting the beam that

provides the largest received power for each RIS. Hence, the UE position is given by the intersection of such two beams. The sum of the normalized received powers from the two RISs (the values are normalized by the maximum received power from each RIS) corresponding to different AoDs are depicted in figure below. The maximum value in this figure represents the estimated UE position (marked by a red star), which is within the 10-cm radius of the ground truth value (marked by a red cross).

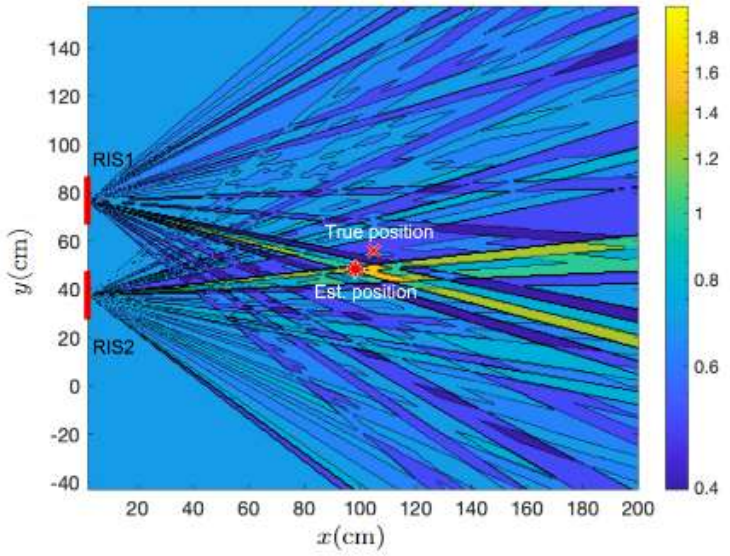


**Figure 5-2. Chalmers V-band RIS for localization measurement result**

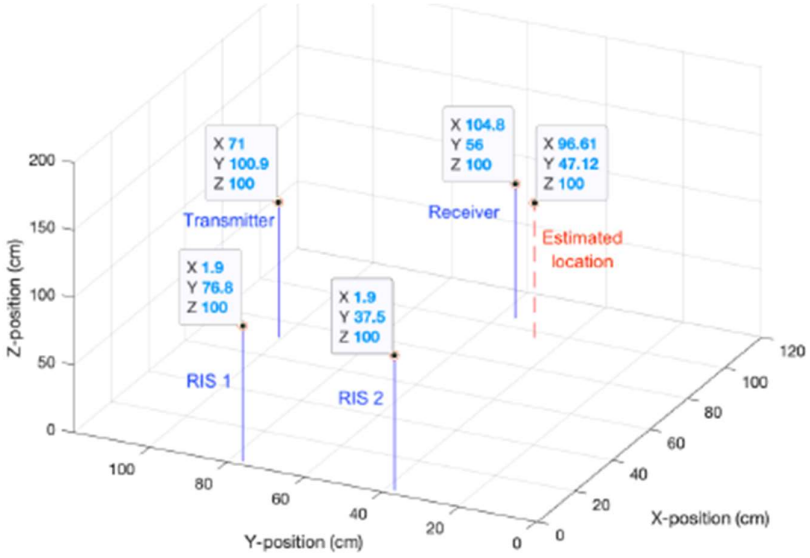


**Figure 5-3. Target position estimation of the measurement setup**

# 6 Conclusions and outlook

In this deliverable, we have presented working progress of all available RIS prototype developments and their performance characterizations. Selected RIS are also test in lab environment for communication use-case and localization use-case. These RIS prototypes developments cover wide frequency range from sub-6GHz to 145 GHz and some RIS prototypes will be selected for planned field trials demonstrations. The available experimental environment and instrumentation for RIS tests are also listed.

# References


| | |
|---|---|
| [AAT16] | V. S. Asadchy, M. Albooyeh, S. N. Tcvetkova, A. Díaz-Rubio, Y. Ra'di, and S. A. Tretyakov, "Perfect control of re-flection and refraction using spatially dispersive metasurfaces," Phys. Rev. B 94, 075142 – 19 August 2016. |
| [DMC21] | Di Lorenzo, P., Merluzzi, M., Strinati, E. C., and Barbarossa, S., "Dynamic Edge Computing empowered by Reconfigurable Intelligent Surfaces," ArXiv:2112.11269, 2021. |
| [AES22] | Albanese, A., Encinas-Lago, G., Sciancalepore, V., Costa-Pérez, X., Phan-Huy, D.-T., & Ros, S., "*RIS-Aware Indoor Network Planning: The Rennes Railway Station Case,"* in Proceedings of the IEEE International Conference on Communications (ICC) 2022, [Online] http://arxiv.org/abs/2201.07591 |
| [MDS21] | P. Mursia, F. Devoti, V. Sciancalepore and X. Costa-Pérez, "RISe of Flight: RIS-Empowered UAV Communications for Robust and Reliable Air-to-Ground Networks," in *IEEE Open Journal of the Communications Society*, vol. 2, pp. 1616-1629, 2021. |
| [MSG21] | P. Mursia, V. Sciancalepore, A. Garcia-Saavedra, L. Cottatellucci, X. C. Pérez and D. Gesbert, "RISMA: Reconfigurable Intelligent Surfaces Enabling Beamforming for IoT Massive Access," in *IEEE Journal on Selected Areas in Communications*, vol. 39, no. 4, pp. 1072-1085, April 2021, doi: 10.1109/JSAC.2020.3018829. |
| [ADS22] | A. Albanese, F. Devoti, V. Sciancalepore, M. Di Renzo, and X. Costa-Ṕerez, "MARISA: A Self-configuring Metasurfaces Absorption and Reflection Solution Towards 6G," in IEEE INFOCOM 2022 - IEEE Conference on Computer Communications, 2022. |
| [HYS20] | H. Lu, Y. Zeng, S. Jin and R. Zhang, "Aerial Intelligent Reflecting Surface: Joint Placement and Passive Beamforming Design With 3D Beam Flattening," in *IEEE Transactions on Wireless Communications*, vol. 20, no. 7, pp. 4128-4143, July 2021 |
| [MFC21] | E. Moro, I. Filippini, A. Capone and D. De Donno, "Planning Mm-Wave Access Networks With Reconfigurable Intelligent Surfaces," *2021 IEEE 32nd Annual International Symposium on Personal, Indoor and Mobile Radio Communications (PIMRC)*, 2021, pp. 1401-1407. |
| [HJU09] | R. Hunger, M. Joham, and W. Utschick, "On the MSE-duality of the broadcast channel and the multiple access channel," IEEE Trans. Signal Process., vol. 57, no. 2, pp. 698–713, Feb. 2009. |
| [PHS05] | C B Peel, B M Hochwald, and A L. Swindelhurst, "A Vector-Perturbation Technique for Near-Capacity Multiantenna Multiuser Communication - Part I: Channel Inversion and Regularization," IEEE Trans. Commun., vol. 53, no. 1, pp. 195–202, Jan. 2005. |
| [SSH04] | Q. H. Spencer, A.L. Swindlehurst, and M. Haardt (2004). Zero-forcing methods for downlink spatial multiplexing in multiuser MIMO channels. *IEEE Transactions on Signal Processing*, *52*(2), 461–471. |

| | |
|---|---|
| [LDY20] | S. Li, B. Duo, X. Yuan, Y. C. Liang, and M. DI Renzo, "Reconfigurable Intelligent Surface Assisted UAV Communication: Joint Trajectory Design and Passive Beamforming," IEEE Wireless Communications Letters, vol. 9, no. 5, pp. 716–720, 2020 |
| [MSB18] | M. Mozaffari, W. Saad, M. Bennis, Y. H. Nam, and M. Debbah, "A tutorial on UAVs for wireless networks: Applications, challenges, and open problems," IEEE Communications Surveys and Tutorials, vol. 21, no. 3, pp. 2334–2360, 2018. |
| [ASC21] | A. Albanese, V. Sciancalepore, and X. Costa-Perez, "SARDO: An Automated Search-and-Rescue Drone-based Solution for Victims Localization," IEEE Transactions on Mobile Computing, pp. 1–12, 2021. |
| [AJH20] | S. Alfattani, W. Jaafar, Y. Hmamouche, H. Yanikomeroglu, A. Yongac ̧oglu, N. D. Đ`ao, and P. Zhu, "Aerial platforms with reconfigurable smart surfaces for 5G and beyond," IEEE Communications Magazine, no. January, pp. 96–102, 2020. |
| [PSZ21] | X. Pang, M. Sheng, N. Zhao, J. Tang, D. Niyato, and K.-K. Wong, "When UAV Meets IRS: Expanding Air-Ground Networks via Passive Reflection," IEEE Wireless Communications, vol. 28, no. 5, pp. 1–7, 2021. |
| [WHA21] | L. Wei, C. Huang, G. C. Alexandropoulos, C. Yuen, Z. Zhang, and M. Debbah, "Channel estimation for RIS-empowered multi-user MISO wireless communications," IEEE Transactions on Communications, vol. 69, no. 6, pp. 4144–4157, June 2021. |
| [ZSA21] | H. Zhang, N. Shlezinger, I. Alamzadeh, G. C. Alexandropoulos, M. F. Imani, and Y. C. Eldar, "Channel estimation with simultaneous reflecting and sensing reconfigurable intelligent metasurfaces," IEEE International Workshop on Signal Processing Advances in Wireless Communications, Lucca, Italy, 27–30 September 2021, pp. 1–6. |
| [SSH22] | K. Stylianopoulos, N. Shlezinger, P. del Hougne, and G. C. Alexandropoulos, "Deep-learning-assisted configuration of reconfigurable intelligent surfaces in dynamic rich-scattering environments," IEEE International Conference on Acoustics, Speech, and Signal Processing, Singapore, 22–27 May 2022, to be presented. |
| [SAH22] | K. Stylianopoulos, G. C. Alexandropoulos, C. Huang, C. Yuen, M. Bennis, and M. Debbah, "Deep contextual bandits for orchestrating multi-user MISO systems with multiple RISs," IEEE International Conference on Communications, Seoul, South Korea, 16–20 May 2022, to be presented. |
| [ASH22] | G. C. Alexandropoulos, K. Stylianopoulos, C. Huang, C. Yuen, M. Bennis, and M. Debbah, "Pervasive machine learning for smart radio environments enabled by reconfigurable intelligent surfaces," IEEE Proceedings, under revision, 2022. |
| [YWL21] | J. Yuan, M. Wen, Q. Li, E. Basar, G. C. Alexandropoulos, and G. Chen, "Receive quadrature reflecting modulation for RIS-empowered wireless communications," IEEE Transactions on Vehicular Technology, vol. 70, no. 5, pp. 5121–5125, May 2021. |
| [CAG22] | K. Chen-Hu, G. C. Alexandropoulos, and A. García Armada, "Non-Coherent MIMO-OFDM uplink empowered by the spatial Diversity in reflecting surfaces," IEEE Wireless Communications and Networking Conference, Austin, USA, 10–13 April 2022, to be presented. |
| [RBF13] | P. Ratajczak, P. Brachat, J. Fargeas and J. Baracco, "C-band active reflectarray based on high impedance surface," 2013 IEEE International Symposium on Phased Array Systems and Technology, 2013, pp. 570-576. |
| [BMB17+] | M. Barazzetta et al., "A Comparison Between Different Reception Diversity Schemes of a 4G-LTE Base Station in Reverberation Chamber: A Deployment in a Live Cellular Network," in IEEE Transactions on Electromagnetic Compatibility, vol. 59, no. 6, pp. 2029-2037, Dec. 2017, doi: 10.1109/TEMC.2017.2657122. |
| [MBM+15] | D. Micheli, M. Barazzetta, F. Moglie and V. Mariani Primiani, "Power Boosting and Compensation During OTA Testing of a Real 4G LTE Base Station in Reverberation |

| | |
|---|---|
| | Chamber," in IEEE Transactions on Electromagnetic Compatibility, vol. 57, no. 4, pp. 623-634, Aug. 2015, doi: 10.1109/TEMC.2015.2434277. |
| [MBC+16] | D. Micheli, M. Barazzetta, C. Carlini, R. Diamanti, V. M. Primiani and F. Moglie, "Testing of the Carrier Aggregation Mode for a Live LTE Base Station in Reverberation Chamber," in IEEE Transactions on Vehicular Technology, vol. 66, no. 4, pp. 3024-3033, April 2017, doi: 10.1109/TVT.2016.2587662. |
| [MBD+18] | D. Micheli et al., "Over-the-Air Tests of High-Speed Moving LTE Users in a Reverberation Chamber," in IEEE Transactions on Vehicular Technology, vol. 67, no. 5, pp. 4340-4349, May 2018, doi: 10.1109/TVT.2018.2795650. |
| [MBB+20] | V. M. Primiani et al., "Reverberation chambers for testing wireless devices and systems," in IEEE Electromagnetic Compatibility Magazine, vol. 9, no. 2, pp. 45-55, 2nd Quarter 2020, doi: 10.1109/MEMC.2020.9133241. |
| [BMD+17] | M. Barazzetta, D. Michel, R. Diamanti, L. Bastianelli, F. Moglie and V. M. Primiani, "Optimization of 4G wireless access network features by using reverberation chambers: Application to high-speed train LTE users," 2016 46th European Microwave Conference (EuMC), 2016, pp. 719-722, doi: 10.1109/EuMC.2016.7824444. |
| [BMG+14] | M. Barazzetta, D. Micheli, P. Gianola, F. Moglie and V. Mariani Primiani, "4G-LTE base station output power estimation from statistical counters during over-the-air tests in reverberation chamber," 2014 International Symposium on Electromagnetic Compatibility, 2014, pp. 284-289, doi: 10.1109/EMCEurope.2014.6930918. |
| [BGM+15] | L. Bastianelli, L. Giacometti, V. M. Primiani and F. Moglie, "Effect of absorber number and positioning on the power delay profile of a reverberation chamber," 2015 IEEE International Symposium on Electromagnetic Compatibility (EMC), 2015, pp. 422-427, doi: 10.1109/ISEMC.2015.7256199. |
| [GHR+10] | E. Genender, C. L. Holloway, K. A. Remley, J. M. Ladbury, G. Koepke and H. Garbe, "Simulating the Multipath Channel With a Reverberation Chamber: Application to Bit Error Rate Measurements," in IEEE Transactions on Electromagnetic Compatibility, vol. 52, no. 4, pp. 766-777, Nov. 2010, doi: 10.1109/TEMC.2010.2044578. |
| [GLL+22] | J.B. Gros, G. Lerosey, F. Lemoult, M. Lodro, S. Greedy, and G. Gradoni. "Multi-path fading and interference mitigation with Reconfigurable Intelligent Surfaces." https://arxiv.org/abs/2206.08290. |
| [LGG+22] | M. Lodro, J.B. Gros, S. Greedy, G. Lerosey, A. Al Rawi, and G. Gradoni. "Experimental Evaluation of Multi-operator RIS-assisted Links in Indoor Environment." https://arxiv.org/abs/2206.07788. |
| [RMG+22] | M. Rossanese, P. Mursia, A. Garcia-Saavedra, V. Sciancalepore, A. Asadi, and X. Costa-Perez, "Designing, Building, and Characterizing RF Switch-based Reconfigurable Intelligent Surfaces", in Proceedings of the 16th ACM Workshop on Wireless Network Testbeds, Experimental Evaluation & Characterization (WiNTECH'22), 2022, Sydney, NSW, Australia. [Online]: http://arxiv.org/abs/2207.07121 |